ACS EARTH AND SPACE CHEMISTRY

http://pubs.acs.org/journal/aesccq

Article

# Electron Transfer Reversibility of Mineral-Associated Organic Matter Dominated by Redox-Active Metastable Substances in a Wetland−Grassland Transition Zone

Xi Zhang, Andreas Kappler, Qian Tian, Jie Jiang,* Zhen Yang,* and Tian ran Sun

Cite This: *ACS Earth Space Chem.* 2026, 10, 1964−1973

Read Online

ACCESS | Metrics & More | Article Recommendations | Supporting Information

**ABSTRACT:** Soil organic matter is redox-active, capable of responding to redox fluctuations, and acts as a biogeobattery to facilitate biogeochemical cycling. However, whether the electron-transfer capacities of mineral-associated organic matter (MAOM) are reversible under controlled chemical redox-switching conditions remains unclear. Mediated electrochemical reduction/oxidation (MER/MEO) analysis showed that MAOM from the transition zones (e.g., between wetland and grassland ecosystems) exhibited the highest electron-accepting and -donating capacities (EAC and EDC) and reversible electron transfer capacity under varying redox states. Specifically, when conditions shift from oxidizing to reducing, the EAC of MAOM decreased in tandem with an equivalent increase in EDC. Conversely, when conditions revert to oxidizing, EAC increased while EDC decreased, demonstrating a fully reversible electron transfer behavior. Multiple complementary analyses reveal that MAOM in the transition zone was enriched in redox-active metastable phases (RAMPs), including redox-active carboxyl functional groups and mineral phases. Mineral phases were the major source of total electron exchange capacity (EEC), whereas organic matter functioned as an important modulator of coupled redox dynamics. MAOM features co-occurrences of iron−carbon (Fe−C) covalent bonding and abundant carboxyl functional groups, as well as mixed-valence iron phases (e.g., green rust and magnetite) and poorly crystalline iron (oxyhydr)oxide minerals (e.g., ferrihydrite and goethite), all of which contribute to electron transfer reversibility. These results suggest that MAOM contains RAMPs that support electron transfer reversibility under varied redox conditions, thereby influencing the overall biogeochemistry and persistence of the soil ecosystem.

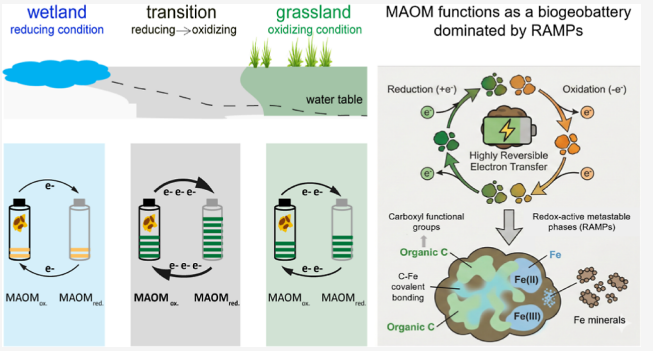


**KEYWORDS:** *mineral-associated organic matter, redox-active metastable substances, electron transfer reversibility, redox fluctuation, electron accepting- and donating capacities*

## 1. INTRODUCTION

Mineral-associated organic matter (MAOM) constitutes 50%−90% of total soil organic matter (SOM) across various landscapes.[1−4] In addition to representing a major and relatively persistent carbon pool, MAOM is increasingly recognized as a redox-active assemblage comprising both organic and mineral components.[5−10] Hydrological changes frequently drive shifts between reducing and oxidizing conditions in soils. Consequently, the redox properties of MAOM are expected to be particularly important in redox-active environments, such as anoxic−oxic interfaces.[11,12] Typical examples include wetland−upland transition zones,[13−15] riparian corridors,[16−18] paddy soils,[19,20] and rhizosphere hotspots.[21,22]

Redox-active carbon moieties[23,24] and iron (Fe)-bearing (oxyhydr)oxide minerals,[25−29] both participate in electron transfer reactions, thereby contributing to soil biogeochemical redox processes. Among mineral phases, poorly ordered or weakly crystalline Fe mineral phases—such as ferrihydrite, goethite, and other metastable Fe phases—have been proposed as typical redox-active metastable phases (RAMPs) capable of both accepting and donating electrons.[30,31] RAMPs have been highlighted in coupled iron−carbon (Fe−C) cycling, where reactive Fe phases regulate Fe−organic matter interactions through electron transfer, complexation, and coprecipitation at redox interfaces.[32] However, it has not been experimentally clarified whether MAOM exhibits reversible electron transfer behavior and maintains stable electron exchange capacities

**Received:** May 14, 2026
**Revised:** July 8, 2026
**Accepted:** July 24, 2026
**Published:** August 4, 2026

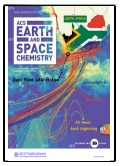





https://doi.org/10.1021/acsearthspacechem.6c00141
*ACS Earth Space Chem.* 2026, 10, 1964−1973

(EEC) during controlled chemical redox-switching treatments across soils with contrasting redox regimes, such as those found in wetlands, grasslands and their transitional zones.

To address this gap, the objectives of this study were (i) to determine whether MAOM can exhibit electron transfer reversibility during a full cycle of oxidization, reduction, and reoxidization and (ii) to elucidate the structural components (i.e., carbon moieties and/or mineral phases) that underpin this redox reversibility. Soil samples were collected along a natural redox gradient, ranging from the underwater area of a wetland region (i.e., reducing conditions) to a grassland region (i.e., oxidizing conditions), including the associated transition zone. To assess the reversibility of MAOM's electron transfer capacities, we subjected the samples to controlled chemical redox shifts: first oxidizing them by exposure to air during extraction processes, then chemically reducing them using $H_2$ in the presence of a Pd catalyst, finally reoxidizing them by exposure to air again. Electron-accepting and -donating capacities (EAC and EDC) of all MAOM samples were quantified using mediated electrochemical reduction/oxidation (MER/MEO) analysis. Additionally, scanning electron microscopy combined with energy-dispersive X-ray spectroscopy (SEM-EDS), X-ray photoelectron spectroscopy (XPS), and X-ray diffraction analysis (XRD) were employed to characterize the compositional and structural features of MAOM. These analyses confirmed that MAOM from the transition zone contains RAMPs characterized by mixed-valence and poorly crystalline Fe minerals, which are intimately associated with the observed reversible electron transfer, highlighting an important role of MAOM acting as a dynamic component that actively participates in soil biogeochemical cycles.

## 2. MATERIALS AND METHODS

### 2.1. Study Sites and Sampling

The soil samples were collected from the Erguna catchment in Inner Mongolia, China. They were collected in July 2024 across a wetland-steppe grassland ecotone (119°42′41.31″ to 120°8′27.73″E, 50°21′10.55″ to 50°32′31.43″N). The sampling sites began at the Erguna wetland and extended southward to the grassland, characterized by a multilayered vegetation system from the wetland to the grassland zone (Figure S1). Within the transition zones, the redox state changed from fully reduced (wetland) to oxidized (grassland) areas, with a variation range of up to 17 km. Dissolved $O_2$ increases with decreasing water table depth from 0.1 ± 0.01 mg/L dissolved $O_2$ in the wetland area to 0.5 ± 0.1−3 ± 0.2 mg/L in the transition zone to 7 ± 1 mg/L in the grassland area. The dominant vegetation species shifted from the wetland ecosystem to the grassland ecosystem (Figure S1). The dominant species in the wetland is ericaceous and woody plants, with sedges across transition sites, and finally Leymus in the grassland (Table S1). All samples were collected from natural, undisturbed areas at least 5 km away from residential zones. Supporting Information provides additional details on the sampling design and sample processing procedures (Figure S1), as well as the climatic characteristics of the study sites (Table S1).

### 2.2. Soil Physicochemical Analysis

Soil-dissolved oxygen was measured in situ by using a dissolved oxygen meter (JPB-607A, Leici, China), with the probe inserted into the original soil at the designated depth. Soil pH was measured by using a calibrated glass electrode in a 1:5 soil-to-water suspension according to the standard method for soil pH determination. Clay content was determined by the pipet method during soil particle size distribution analysis, based on sedimentation of dispersed soil particles and timed sampling at a fixed depth.[33]

Milled subsamples (0.147 mm) were analyzed for total N concentrations using a Vario Max and a Vario EL (Elementar Analysensysteme GmbH), respectively. Total C and inorganic carbon were determined using a total organic carbon (TOC) analyzer (TOC-L, SHIMADZU). Total Fe, magnesium (Mg), Silicon (Si), and aluminum (Al) were determined by inductively coupled plasma-optical emission spectrometry (ICP-OES, Thermo Scientific iCAP 7200 Duo). Free oxides of Fe and Al in soils were extracted using the dithionite-citrate-bicarbonate method (DCB).[34,35] For Fe oxides, we analyzed the amount of poorly crystalline Fe and more crystalline Fe. Poorly crystalline Fe was extracted with an ammonium oxalate-oxalic acid solution (pH 3, solid-to-solution ratio of 1:50).[12] More crystalline Fe was extracted with 6 M HCl at 70 °C for 24 h.[36,37] The Fe concentrations in all extracts were subsequently determined by an atomic absorption spectrophotometer (AA6880).

### 2.3. SOM Fractionation Preparation and Chemical Analysis

Solid phase SOM fractionation was grouped using the density separation technique by sodium iodide (NaI). Briefly, air-dried and sieved (<2 mm) soil samples (10 g) were shaken in 34 mL of 1.85 g $cm^{-3}$ NaI (AR 99.5%, Shanghai Macklin Biochemical Co., Ltd., Shanghai, China).[38] The completely mixed solution was sonicated and centrifuged (1800g, 15 min). The supernatant dispersed soil solution was filtered through a glass microfiber (GF/C) filter with a 125 mm diameter (Whatman, 1825−125). The organic material retained on the filter and oven-dried (50 °C) was defined as light POM. The remaining sediment (heavy fraction residue) after centrifugation was subsequently sieved through a 53 $\mu$m mesh to separate heavy POM (>53 $\mu$m) from MAOM (<53 $\mu$m).[39] Particulate organic carbon (POC) and mineral-associated organic carbon (MAOC) make up the majority of TOC (up to 95%) across all samples (Figure 1a). The mass recovery of POM and MAOM is up to 98% (Figure S2a).

### 2.4. Mineralogical Characterization

The surface chemical constituents and element states (C-species and Fe-species of MAOM) were determined by X-ray photoelectron spectroscopy (XPS, ESCALAB MARKII, VG, UK). The measurements were performed under a base pressure of $5 \times 10^{-10}$ Pa. The X-ray source was Al K$\alpha$ ($h\nu$ = 1486.68 eV) with a working voltage of 15 kV and filament current of 10 mA, and signals were accumulated over 5−10 cycles. The pass energy was set to 50 eV with a step size of 0.1 eV. The spectra were recorded and analyzed using Avantage software, and the binding energies were calibrated to the C 1s peak at 284.80 eV. A Shirley background was applied before peak fitting, and the peaks were fitted using a mixed Gaussian−Lorentzian line shape.

Sample morphology and elemental distributions were examined by a field-emission scanning electron microscope (FE-SEM, ZEISS Supra 55VP or equivalent) equipped with a silicon drift detector energy-dispersive X-ray spectroscopy (SDD-EDS) system (e.g., Bruker QUANTAX XFlash 6|60). Air-dried subsamples were mounted on Al stubs and gold-coated (~5 nm) to minimize charging. Secondary electron images were acquired at 3−5 kV, and EDS maps (C and Fe) were collected at 15 kV under high vacuum.

Each MAOM fraction was air-dried, finely ground, and analyzed using an X-ray diffractometer (X'Pert 3 powder, PANalytical, Netherlands) equipped with Cu K$\alpha$ radiation ($\lambda$ = 1.5406 Å). Measurements were performed over a 2$\theta$ range of 10−90° with a step size of 0.05°. Mineral identification of MAOM fractions was conducted using MATCH!4 software (Crystal Impact, Bonn, Germany), and semiquantitative analysis of phase composition was performed based on the reference database provided by the software.

### 2.5. A Cycle of Redox Oscillations of MAOM

MAOM fractions extracted from the wetland were exposed to air during fractionation and therefore partially oxidized prior to the experiments. This study focuses on the electron transfer behavior of MAOM during a controlled chemical redox-switching sequence (oxidizing-reducing-reoxidizing), not really on the initial redox states (from reducing or oxidizing). Therefore, the extracted samples exposed to air were used as the oxidized starting state for subsequent experiments, and this does not affect the evaluation of electron transfer reversibility during the redox cycle.





https://doi.org/10.1021/acsearthspacechem.6c00141
ACS Earth Space Chem. 2026, 10, 1964−1973

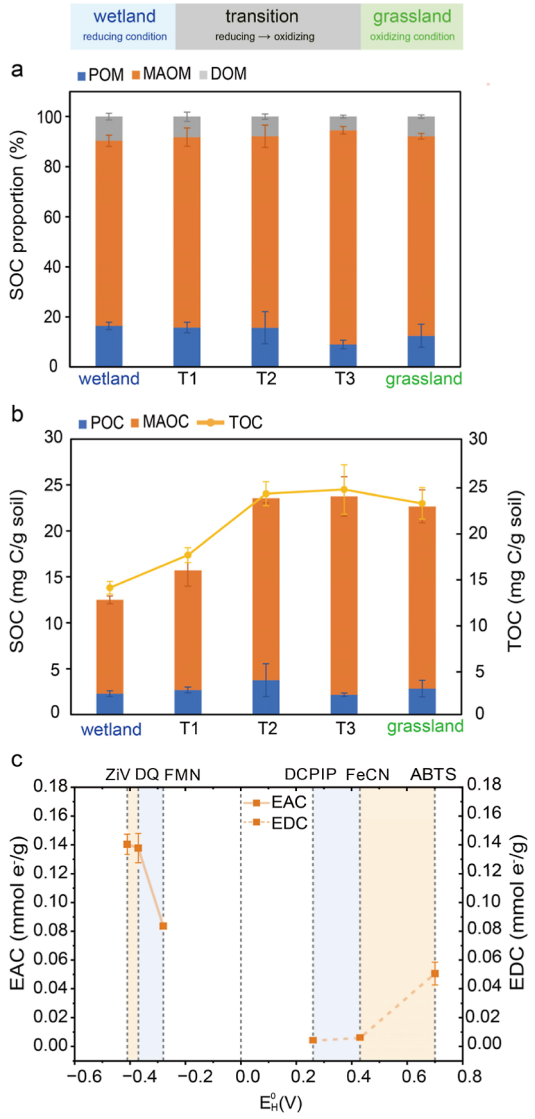


**Figure 1.** Distribution, accumulation, and redox characteristics of mineral-associated organic matter (MAOM) across wetland and grassland ecosystems and the associated transition zone. (**a**) Soil organic carbon (SOC) fractionation proportion. (**b**) SOC composition of particulate organic carbon (POC), mineral-associated organic carbon (MAOC), and dissolved organic carbon (DOC) across wetland and grassland ecosystems and the associated transition zone. (**c**) Electron-accepting and -donating capacities (EAC and EDC) of MAOM in the transition zone determined at different applied redox potentials. This analysis was probed with a suite of redox mediators, including zwitterionic viologen 4,4′-bipyridinium-1,1′-bis(2-ethylsulfonate) (ZiV), diquat dibromide monohydrate (DQ), riboflavin 5′-monophosphate sodium salt hydrate (FMN), 2,6-dichlorophenolindophenol sodium salt hydrate (DCPIP), potassium ferricyanide ($K_3Fe(CN)_6$), and 2,2′-azino-bis(3-ethylbenzothiazoline-6-sulfonic acid) diammonium salt (ABTS). The redox potentials of these mediators were determined under standard conditions (pH 7.0, 25 °C) at a scan rate of 20 mV $s^{-1}$.

All MAOM samples were subjected to a redox-switching treatment consisting of chemical reduction by $H_2$ in the presence of a Pd catalyst (palladium-coated alumina pellets, 0.5% Pd, Merck) as reported by previous studies,[40−42] followed by reoxidation upon exposure to air. Specifically, 30 mg of MAOM was weighed into a serum vial (5 mL) and suspended in 3 mL of deoxygenated water inside an anaerobic glovebox. The vials were than evacuated and flushed with $H_2$ gas. Based on preliminary tests, an $H_2$ flushing time of 15 min was sufficient to achieve the reduced state (Figure S3). After the reduction treatment, the palladium-coated alumina pellets were physically removed from the serum vial inside an anaerobic glovebox. For reoxidation, the reduced suspensions were subsequently exposed to air for 18 h. Before transferring the suspensions back into the glovebox, $O_2$ and $H_2$ in the headspace were removed by purging with 99.999% $N_2$ gas for at least 30 min.

## 2.6. Electrochemical Materials and MER and MEO Analysis

The redox mediators were used in the MER/MEO analyses (Table S2). These mediators span a range of formal redox potentials to probe electron transfer properties of MAOM (Figure 1c). In addition, zwitterionic viologen 4,4′-bipyridinium-1,1′-bis(2-ethylsulfonate) (ZiV) and 2,2′-azino-bis(3-ethylbenzothiazoline-6-sulfonic acid) diammonium salt (ABTS) were further used for the quantitative determination of EAC and EDC of MAOM under different redox conditions (Figures 2 and 3).

Electrochemical analysis was controlled using a potentiostat (Bio-Logic SAS, VSP-3e, France). Potentials were set versus an Ag/AgCl references electrode but are reported versus the standard hydrogen electrode (SHE). Mediated electrochemical experiments were carried out in electrochemical cells as reported by previous studies.[43,44] Briefly, mediated electrochemical experiments containing 5 mL of a carrier stream (0.1 M phosphate buffer and 0.1 M KCl at pH 7), a cylindrical glassy carbon working electrode (WE), a Pt wire counter electrode separated from the WE compartment by a glass frit, and an Ag/AgCl reference electrode were conducted. All MER/MEO experiments were conducted in a pH 7 buffered electrolyte solution (0.1 M phosphate, 0.1 M KCl). All electrochemical analyses were conducted in an anoxic glovebox (<1 ppm of $O_2$) with an $N_2$ atmosphere (Vigor, LG1200/750TS, China). All aqueous solutions were purged with 99.999% $N_2$ gas and degassed overnight in an anoxic chamber before being transferred into the glovebox. To validate the selection of the buffer solution, comparative experiments of the electron transfer capacity of MAOM in different buffer systems were performed. The comparison showed that EAC and EDC values in the 3-(*N*-morpholino)propanesulfonic acid (MOPS) system were slightly lower than those in the phosphate system, as shown in Figures S4 and S5. This indicates that the phosphate buffer affects the absolute values—likely due to its interactions with Fe/Al (oxyhydr)-oxide surfaces, weakening mineral−organic associations in MAOM. However, the difference was small and the overall trend was consistent. Thus, although phosphate may influence the Fe/Al-associated component in MAOM, it does not influence the relative tendency between samples or the main conclusions in this study.

We quantified the $Q_{EAC}$ and $Q_{EDC}$ values of MAOM at strongly reducing ($E_H$ = −0.687 V) and strongly oxidizing ($E_H$ = +0.610 V) redox potentials, respectively. To quantify the EAC of MAOM, MER was performed by spiking $ZiV^{2+}$ into the electrochemical cell (10 mM, 100 μL); $ZiV^{2+}$ was reduced to $ZiV^{\bullet+}$ at the WE, resulting in a reductive current response. The EDC of MAOM was measured by MEO with an experiment setup similar to MER, except that $ABTS^{2-}$ was oxidized to $ABTS^{\bullet-}$ at the WE. MAOM suspensions (100 μL) were then spiked into the electrochemical cell. After each measurement, the electrochemical cell was emptied, rinsed thoroughly with deionized water, and refilled with fresh electrolyte solution before the next run. Peak integration of the current response yielded the number of electrons transferred between MAOM and the working electrode via the redox mediator (eq 1)

$$q = \frac{1}{F}\int_{t1}^{t2} I\,\mathrm{d}t \tag{1}$$

where q is the number of electrons transferred in moles, $F$ is the Faraday constant (96,485 C/mol), and $t$ is time. Cyclic voltammetry (CV) experiments of mediators were conducted in a 10 mL solution of buffer containing a 3 mm diameter glassy carbon disk working electrode, a platinum wire counter electrode, and an Ag/AgCl reference electrode. Supporting Information (Figure S6) presents representative CV curves of the six redox mediators together with the




https://doi.org/10.1021/acsearthspacechem.6c00141
ACS Earth Space Chem. 2026, 10, 1964−1973

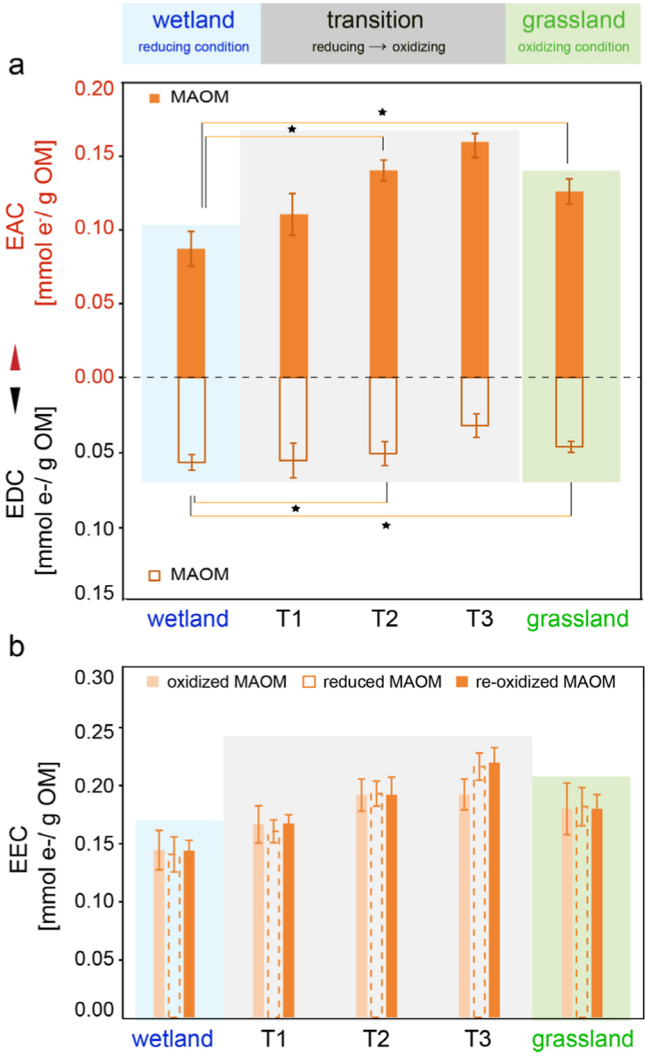


**Figure 2.** Electrochemical properties of mineral-associated organic matter (MAOM) across wetland and grassland ecosystems and the associated transition zone. (**a**) Electron-accepting and -donating capacities (EAC and EDC) of MAOM under the oxidized conditions (EAC and EDC were quantified by mediated electrochemical reduction/oxidization (MEO/MER) analysis using 4,4′-bipyridinium-1,1′-bis(2-ethylsulfonate) (ZiV) and 2,2′-azino-bis-(3ethylbenzothiazoline-6-sulfonic acid) diammonium salt (ABTS) as the redox mediators, respectively). (**b**) Electron exchange capacities (EEC, the sum of EAC and EDC) of MAOM during redox fluctuations (including oxidized, reduced, and reoxidized states). Units are expressed per gram of dry MAOM (mmol $e^-$/g). Error bars represent the standard error from triplicates. * indicates $p < 0.05$, and unmarked indicates no significant difference.

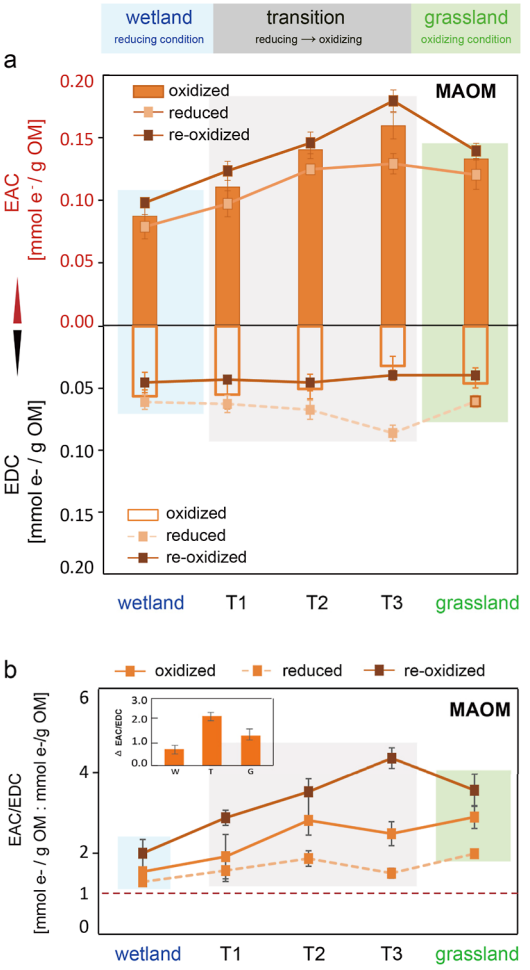


**Figure 3.** Electrochemical characteristics of mineral-associated organic matter (MAOM) under redox fluctuations in wetland and grassland areas and their transition zone. (**a**) Electron-accepting and -donating capacities (EAC and EDC) of MAOM during redox fluctuations (from an oxidized state to a reduced state and back to a reoxidize state). (**b**) Variations in the EAC/EDC ratio of MAOM across different redox states. The EAC/EDC ratio reflects the net redox balance of the MAOM pool, where higher values indicate a more oxidized state (predominance of EAC) and lower values indicate a more reduced state (predominance of EDC). Δ(EAC/EDC), calculated as ([EAC/EDC]reoxidized - [EAC/EDC]reduced), quantifies the magnitude of the shift in the net redox balance during controlled redox perturbation. A larger Δ(EAC/EDC) therefore signifies greater electron redistribution between EAC and EDC, indicating a stronger responsiveness of MAOM to changes in redox conditions. Accordingly, Δ(EAC/EDC) serves as an indicator of the redox sensitivity of MAOM. Units are expressed per gram of dry MAOM (mmol $e^-$/g). Error bars represent the standard error from triplicates.

experimental conditions and the measured standard redox potentials ($E_H^0$).

### 2.7. Quantitative Partitioning of Organic and Mineral Contributions to the EEC of MAOM

To quantitatively estimate the respective contributions of organic matter and mineral phases to the measured EEC of MAOM, EEC values were normalized to both total MAOM mass (mmol $e^-$/g MAOM) and organic carbon mass within MAOM (mmol $e^-$/g MAOC). The calculation assumes that, if the measured EEC of MAOM originated exclusively from its organic component, then the expected EEC per gram of MAOM should equal the product of the MAOC-normalized EEC and the organic carbon mass fraction of the corresponding MAOM sample. The mineral-phase contribution (notably Fe-bearing minerals) to the overall electron transfer capacity was calculated as mineral = $EEC_{MAOM}$ - ($EEC_{MAOC} \times f_{oc}$), where $f_{oc}$ is the mass fraction of organic carbon in MAOM The relative mineral contribution can then be expressed as the difference in EEC between total mineral-organo EEC and organic-derived EEC.

## 3. RESULTS

### 3.1. Carbon Distribution and Redox Potential Range of MAOM along the Wetland-to-Grassland Gradient

The distribution of soil organic carbon (SOC) exhibited distinct patterns in solid phase SOM fractions. In all sites,





https://doi.org/10.1021/acsearthspacechem.6c00141
ACS Earth Space Chem. 2026, 10, 1964−1973

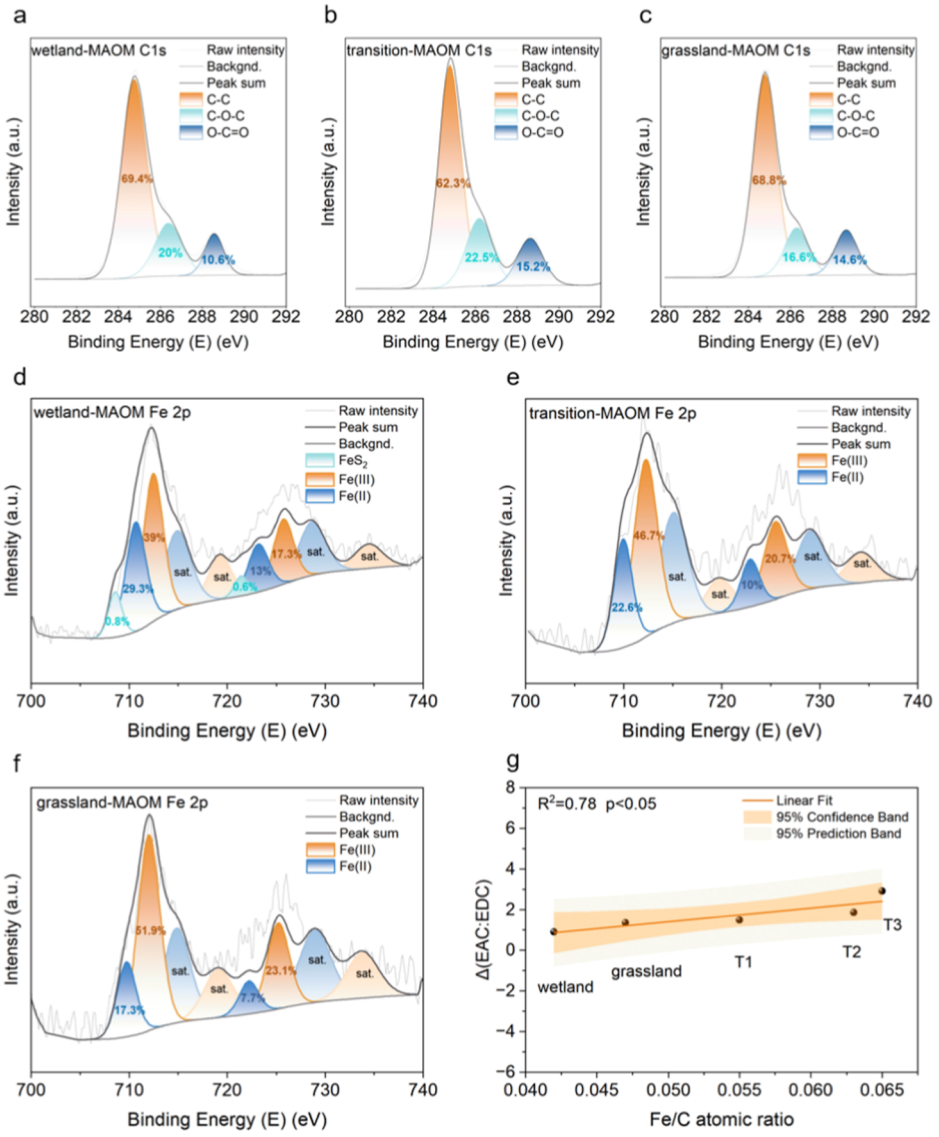


**Figure 4.** X-ray photoelectron spectroscopy (XPS) characterization of carbon (C) functional groups and iron (Fe) minerals in mineral-associated organic matter (MAOM) across the wetland, transition zone, and grassland. (**a**–**c**) C 1s XPS spectra of MAOM in the wetland, transition zone, and grassland. (**d**–**f**) Fe 2p XPS spectra of MAOM and (**g**) correlation between Fe/C atomic ratio and Δ(EAC/EDC) of MAOM across reduced and reoxidized states in the wetland, transition zones, and grassland ($R^2$ = 0.78, $p$ < 0.05).

MAOC accounted for approximately 70−80% of total SOC, dominating the SOC, while POC contributed only a small fraction (<20%), and DOM remained very low (Figure 1a). This indicates that along the wetland-to-grassland gradient, the SOC pool was primarily dominated by MAOM. Notably, MAOC reached its highest content in the transition zone (22.34 ± 1.99 mg C/g soil), exceeding those in wetland (9.18 ± 0.96 mg C/g soil) and grassland (19.83 ± 1.78 mg C/g soil) (Figure 1b). Furthermore, clear differences in soil physico-chemical and mineralogical properties were observed among ecosystems along the gradient. Specifically, the transition zone exhibited lower pH (5.43 ± 0.16) than the wetland (6.08 ± 0.03) and grassland soils (6.18 ± 0.03), while its clay content (244 ± 29 g/kg) was higher than that of the other two ecosystems (wetland: 121 ± 7 g/kg; grassland: 238 ± 5 g/kg) (Table S3). In addition, the transition zone exhibited higher concentrations of free Fe/Al oxides (Fe: 3.34 ± 0.30 g/kg; Al: 2.05 ± 0.34 g/kg) (Table S3), with poorly crystalline Fe (2.75 ± 0.35 g/kg) reaching its highest level among the three ecosystems, exceeding those in both the wetland (2.11 ± 0.04 g/kg) and grassland (2.45 ± 0.19 g/kg) soils (Figure S8c).

The redox potential range over which electron transfer occurred in the MAOM samples was examined using a suite of mediators spanning −0.41 to +0.68 V. EAC was the highest at the reducing end with ZiV (−0.41 V) and DQ (−0.37 V) and declined toward FMN (−0.28 V), whereas EDC remained low at +0.26 V (DCPIP) to +0.43 V (ferri/ferrocyanide) but increased sharply with ABTS (+0.68 V) (Figure 1c).

### 3.2. Electron-Accepting and -Donating of MAOM during a Cycle of Redox Oscillations

In all samples, MAOM accounted for over 70% of the total SOM (Figure 1a). Electrochemical analysis showed that for all oxidized samples, MAOM exhibited higher EAC (0.087 ± 0.012 to 0.160 ± 0.010 mmol $e^-$/g MAOM) than EDC (0.032 ± 0.008 to 0.056 ± 0.005 mmol $e^-$/g MAOM) (Figure 2a). Notably, both EAC and EDC of MAOM were generally higher in the transition zone than that in wetland and grassland


https://doi.org/10.1021/acsearthspacechem.6c00141
ACS Earth Space Chem. 2026, 10, 1964−1973

(Figure 2a), suggesting enhanced redox activity of MAOM in the transition zone. When examined in more detail, the three transition-zone sites (T1-T3) showed a clear environmental gradient, with dissolved oxygen increasing progressively from T1 to T3 (Table S3). Correspondingly, the EAC of MAOM also increased along this sequence, whereas the EDC showed no significant differences among T1-T3 (Figure 2a), indicating that MAOM redox properties changed along the internal environmental gradient of the transition zone. The increase in dissolved oxygen from T1 to T3 reflects progressively more oxidizing conditions, which likely enhance the abundance or stability of electron-accepting components in MAOM, thereby contributing to the higher EAC observed at sites with higher dissolved oxygen.

The total electron exchange capacity (EEC, the sum of EAC and EDC) of MAOM was normalized to both total MAOM mass (mmol $e^-$/g MAOM) and MAOM organic carbon mass (mmol $e^-$/g MAOC) to quantify the respective contributions of organic matter and mineral phases. Organic matter accounted for approximately 40−45% of the total EEC across all MAOM samples, whereas mineral phases contributed approximately 55%−60% (Figure S13).

The EEC for all MAOM samples at different redox states (e.g., oxidized, reduced, and reoxidized states) remained stable (Figures 2b and S7). Specifically, within the transition zone, when changing from oxidizing to reducing conditions, EAC significantly ($p < 0.05$) decreased by 0.021 ± 0.001 mmol $e^-$/g MAOM, while EDC significantly increased by 0.029 ± 0.002 mmol $e^-$/g MAOM (Figure 3a). When conditions were switched from reducing back to oxidizing, EAC significantly increased by 0.032 ± 0.008 mmol $e^-$/g MAOM, whereas EDC decreased by 0.030 ± 0.011 mmol $e^-$/g MAOM (Figure 3a).

Although the EEC in MAOM remained stable during the changes in redox states, the ratio between EAC and EDC changed for each sample (i.e., reflecting by a EAC/EDC ratio) (Figure 3b). For the MAOM isolated from the transition zone, the variances in EAC/EDC ratios between reduced and reoxidized states were 2.1 ± 0.3 for MAOM samples (Figure 3b), compared to wetland (0.9 ± 0.2 for MAOM) and grassland (1.5 ± 0.5 for MAOM) (Figure 3b).

### 3.3. Characterization of Fe−C in MAOM along the Wetland-to-Grassland Gradient

The Fe speciation analysis result revealed that the content of poorly crystalline Fe phase in the transition zone (2.75 ± 0.35 g/kg) was also higher than that in wetland (2.11 ± 0.04 g/kg) and grassland (2.45 ± 0.19 g/kg) (Figure S8c). The XPS analysis further revealed the specific chemical states of carbon and iron in MAOM across the three ecosystems. For the C 1s spectra (Figure 4a−c), the main peaks were deconvoluted into three components: C−C (284.8 eV), C−O−C (286.4 eV), and O−C═O (288.5 eV). The relative abundance of C−C, representing aliphatic carbon, was the highest in the wetland MAOM (69.4%), followed by the grassland (68.8%) and the transition zone (62.3%). In contrast, the transition zone MAOM exhibited the highest proportion of oxygen-containing functional groups, with C−O−C (22.5%) and O−C═O (15.2%) collectively accounting for 37.7% of the total carbon, which was significantly higher than that in the wetland (30.6%) and grassland (31.2%) (Figure 4a−c). This indicated a higher degree of carbon oxidation in the transition zone MAOM.

For the Fe 2p spectra (Figure 4d−f), two main peaks corresponding to Fe 2p3/2 and Fe 2p1/2 were observed, accompanied by a certain degree of satellite peaks. Given the complexity of Fe 2p spectra, the semiquantitative estimates of Fe(II)/Fe(III) ratios followed the order wetland MAOM > transition-zone MAOM > grassland MAOM (Table S6), suggesting a possible relative decrease in Fe(II)-related spectral contributions along the wetland-to-grassland gradient, which was consistent with the increasing aeration and redox potential along this gradient.

In addition, the Fe/C atomic ratio (%) was comparably low in both wetland (0.42) and grassland MAOM (0.47) but was significantly higher in the transition zone, reaching 0.63 (Table S5). A significant positive correlation was observed between the Fe/C atomic ratio and Δ(EAC/EDC) of MAOM across reduced and reoxidized states ($R^2 = 0.78$, $p < 0.05$, Figure 4g).

In all samples, SEM-EDS mapping showed spatial colocalization of C and Fe, with the most pronounced overlapping C and Fe signals observed in the transition-zone MAOM (Figures S10−11). XRD analysis showed that MAOM in the transition zone contained amorphous/poorly crystalline Fe phases and mixed-valence Fe minerals, including ferrihydrite, goethite, green rust, and magnetite (Figure S12). Additionally, MAOM in the wetland contained a small amount of the Fe(II) phase (e.g., $FeS_2$), whereas MAOM in the grassland contained crystalline Fe(II)-bearing silicates, including enstatite ferroan ($Fe_{0.155}Mg_{0.845}O_3Si$) and ferrobustamite ($CaFeO_6Si_2$) (Figure S12).

## 4. DISCUSSION

### 4.1. The Electron transfer Reversibility of MAOM Is Dominated by RAMPs

Along the wetland-to-grassland gradient, the SOC pool was primarily dominated by MAOM, with MAOC reaching its highest content in the transition zone (Figure 1a and b). The variation in carbon storage of MAOM across ecosystems reflects differences in redox dynamics along the gradient. Additionally, the transition zone was characterized by lower pH, higher clay content, greater concentrations of free Fe/Al oxides (Table S3), and a poorly crystalline Fe phase (Figure S8c). These environmental conditions likely promoted the stabilization of organic carbon through enhanced mineral−organic associations. Specifically, lower pH enhances organic carbon binding to mineral surfaces, while higher clay content provides additional surface area. Free Fe/Al oxides offer reactive sites for carbon stabilization, and poorly crystalline Fe minerals are particularly effective at retaining organic carbon through adsorption and coprecipitation.

The electron-transfer reversibility of MAOM was demonstrated by electrochemical analysis. The total EEC of MAOM remained conserved during reduction and subsequent reoxidation, with electrons being reversibly repartitioned between the electron-accepting and electron-donating pools (Figure 3a). This indicates that redox-active moieties embedded within MAOM can be "charged" and "discharged" during controlled chemical redox shifts, consistent with a previous study showing that SOM (e.g., POM) from peatlands can exhibit reversible electron-transfer behavior.[45] Previous studies have shown that carbon functional groups are responsible for such reversibility. For example, humic substances contain quinone/phenolic moieties that confer both EAC and EDC.[46−49] MAOM in the transition zone exhibited high EAC and EDC, as well as larger redox-driven shifts in the EAC/EDC ratio between reduced and reoxidized




https://doi.org/10.1021/acsearthspacechem.6c00141
ACS Earth Space Chem. 2026, 10, 1964−1973

states (i.e., high redox sensitivity). These features suggest that MAOM in the transition zone possessed high redox activity and electron transfer reversibility. Compared with wetland and grassland soils, the transition zone is characterized by more dynamic redox conditions, which likely promote the preservation of redox-active organic moieties and mineral−organic associations, thereby contributing to the higher EEC of MAOM. Mineral-dominant contribution to MAOM's EEC: mechanistic insights. Quantitative partitioning reveals that mineral phases, particularly redox-active metastable Fe minerals, contribute the majority (55−60%) of MAOM's total EEC. RAMPs undergo reversible Fe(III)/Fe(II) solid phase transformations, serving as a dynamic electron reservoir. Organic matter plays a secondary but critical role by providing quinone/phenolic redox groups, stabilizing metastable Fe minerals against irreversible transformation, and modulating mediator accessibility. Thus, the coupled OM-Fe redox dynamics constitute the functional unit of MAOM. The highest EEC and redox sensitivity observed in transition-zone MAOM arise from the coexistence of preserved organic moieties and abundant RAMPs under fluctuating redox conditions. These findings extend the traditional OM-centric view, demonstrating that in mineral-rich systems, mineral phases can dominate electron exchange capacity while organic matter remains essential for carbon stabilization and microbial electron shuttling.

MAOM in the transition zone was characterized by more abundant poorly crystalline Fe (Figure S8c), higher Fe/C ratios (Table S5), and mixed-valence Fe environments (Figure 4d−f), suggesting the presence of redox-active, metastable Fe−C species. In addition, Fe/C ratios showed a positive correlation with the changes in EAC/EDC between reduced and reoxidized states ($R^2 = 0.78$, $p < 0.05$, Figure 4g). Building upon the quantitative dominance of mineral phases in the EEC, we further examined the mechanistic role of Fe abundance relative to organic carbon. Redox-active metastable Fe minerals (e.g., ferrihydrite and magnetite) associated with organic matter likely act as a dynamic electron buffer or shuttle. When Fe/C is higher, a larger pool of these Fe phases is present, relative to organic carbon. During reduction, these Fe phases can be preferentially reduced, consuming electrons and thereby altering the distribution of electron equivalents between the mineral and organic moieties. Upon reoxidation, they can be reoxidized, further modulating the EAC/EDC balance. Thus, higher Fe/C may enhance the overall redox flexibility of the MAOM composite, leading to a greater shift in the EAC/EDC in response to redox changes. In this study, SEM-EDS mapping revealed Fe−C colocalization within MAOM in the transition zone (Figure S11). XPS spectra demonstrated enriched carboxyl functional groups (Figure 4a−c), and XRD identified poorly crystalline Fe minerals such as ferrihydrite, goethite, green rust, and magnetite (Figure S12). These observations indicated that MAOM was dominated by a redox-active metastable phase, contributing to the electron-transfer reversibility of MAOM.

RAMPs represent metastable Fe (III)-oxyhydroxides intimately coupled with carboxyl-rich organic moieties, enabling bidirectional electron transfer. Reduced MAOM accept electrons, leading to partial Fe reduction and organic protonation; upon reoxidation, stored electrons are released, restoring the original Fe-organic assemblies. This reversible "charge−discharge" behavior allowed MAOM to serve as recyclable electron shuttles. Importantly, the MAOM dominated by RAMPs lowers kinetic barriers to electron transfer and prevents Fe passivation, thereby sustaining long-term redox recyclability.[32] Consequently, redox-active metastable MAOM are able to play a critical role in coupling Fe and C cycles in redox-dynamic environments (e.g., transition zones),[32,50] simultaneously influencing greenhouse gas emissions[51−54] and organic carbon persistence.

### 4.2. The Role of Redox-Active Metastable MAOM in Redox-Dynamic Conditions

Although the total EEC of MAOM remained largely conserved during the controlled redox-switching experiment, indicating reversible electron-transfer behavior (Figure 3a), substantial redistribution occurred between the electron-accepting and electron-donating pools. We propose that this apparent stability reflects an operational feature of our experimental design, a short-term controlled chemical perturbation rather than a demonstration of indefinite stability. Within this operational context, the stability of mediator-accessible EEC arises from at least three nonmutually exclusive mechanisms: (i) compensatory effects between organic and mineral pools: redox fluctuations may alter specific organic functional groups (i.e., quinone/hydroquinone and phenolic groups) and Fe phases, but the net pool of electron-exchangeable moieties accessible to the mediators may remain approximately conserved over a single short-term cycle; (ii) rapid reversibility of RAMPs: metastable Fe minerals (e.g., ferrihydrite or magnetite) present in MAOM undergo solid-phase Fe(II)/Fe(III) cycling without significant dissolution or irreversible redox transformations, allowing them to function as reversible electron buffers, and (iii) mediator accessibility as an operational filter: the measured EEC values reflect the capacity of MAOM to exchange electrons with the added mediators, probing only a subset of the total redox-active pool, which may be kinetically or thermodynamically not accessible under the measurement conditions.

MAOM in the transition zone exhibited high redox sensitivity, as evidenced by substantial redox-active shifts in the EAC/EDC ratio between reduced and reoxidized states (i.e., high redox sensitivity) (Figure 3b). Additionally, the EAC of MAOM was the highest at the reducing end with −0.41 V and −0.37 V and declined toward −0.28 V, whereas EDC of MAOM remained low at +0.26 V to +0.43 V but increased sharply at +0.68 V (Figure 1c). These results indicate that MAOM in redox-dynamic soil conditions possessed a continuous distribution of redox-active functional groups spanning approximately −0.41 V to +0.43 V, rather than discrete groups with fixed potentials. This broad redox potential range enables MAOM to act as a reversible electron acceptor and donor, continuously buffering redox changes during alternating reduction and oxidation. Consequently, this buffering effect modulates microbial respiration and nutrient transformation,[55−58] and also enhances MAOM persistence: reversible electron transfer mitigates complete mineralization of MAOM under redox fluctuations, thereby contributing to its long-term retention in soils.[59,60] Thus, redox-active metastable MAOM is not merely a passive intermediate of organic matter turnover but a dynamic component that actively participates in soil biogeochemical cycles.

Higher Fe/C ratios (Table S5) and mixed-valence Fe environments (Figure 4d−f) suggest the presence of redox-active, metastable Fe−C species. These association are directly shaped by frequent redox oscillations: drying introduces




https://doi.org/10.1021/acsearthspacechem.6c00141
ACS Earth Space Chem. 2026, 10, 1964−1973

oxygen, driving Fe (II) oxidation; wetting creates anoxia, promoting Fe (III) reduction. Unlike permanently reducing or oxidizing soils, where Fe tends to form stable crystalline oxides or fully reduced sulfides with limited capacity for dynamic interaction with organic carbon, the recurring fluctuations in transition zones continuously regenerate reactive mixed-valence Fe (Figure S12). Such Fe forms relatively weak but reversible bonds with organic carbon, maintaining MAOM in a metastable state. On the one hand, this state enables sustained carbon stabilization through repeated adsorption and coprecipitation,[61−63] while simultaneously preserving a carbon pool that remains accessible to microbial respiration upon shifts in redox conditions.[63−66] On the other hand, redox fluctuations promote the formation of persistent MAOM rather than driving extensive carbon loss, as the dynamic Fe−C interactions rebuild protection, with only a small proportion of labile carbon in each redox cycle.[25,67] This dual capacity reconciles the apparently contradictory observations that concurrent carbon accumulation and active carbon turnover, which would be expected to occur frequently, are often reported in redox-dynamic transition zones in ecosystems.

## 5. CONCLUSIONS

This study provides direct evidence that MAOM shows reversible electron-transfer capacity during controlled chemical redox-switching treatments. Structural characterizations indicate that the enhanced electron-transfer capacity and redox sensitivity of MAOM in transition zones are associated with the presence of RAMPs. This allows MAOM to act as a dynamic electron reservoir, facilitating bidirectional electron transfer at microbial−mineral−organic interfaces. It regulates Fe−C cycling and maintains the dynamic equilibrium of biogeochemical processes, enhancing the transformation efficiency of carbon and other elements in soils under changing environmental conditions.

## ■ ASSOCIATED CONTENT

### Supporting Information

The Supporting Information is available free of charge at https://pubs.acs.org/doi/10.1021/acsearthspacechem.6c00141.

Descriptions of the study site and sampling procedures, dissolved $O_2$ distribution, and dominant vegetation; mass proportions and carbon contents of POM and MAOM; optimization of $H_2$ flushing time for MAOM reduction; comparison of EAC and EDC measured using phosphate and MOPS buffer systems; evaluation of phosphate buffer effects on redox potential measurements; cyclic voltammograms, experimental conditions, and measured redox potentials of the redox mediators; EEC of MAOM during redox fluctuations; bulk soil physicochemical properties, elemental composition, and Fe speciation; XPS characterization of MAOM; SEM images of MAOM; SEM coupled with EDS elemental maps (Fe and C) of MAOM; XRD characterization of MAOM; EAC and EDC normalized to organic carbon and organic matter mass; climatic characteristics and dominant vegetation from wetland to grassland and the associated transition zones; redox mediators used in the MEO/MER analyses; soil physicochemical properties from wetland to grassland and the associated transition zones; deconvoluted C 1s XPS peak assignments and relative proportions of C−C, C−O−C, and O−C═O functional groups in MAOM; surface elemental composition (at. %) and Fe/C atomic ratios of MAOM; and relative proportions of Fe(II), Fe(III), and $FeS_2$ derived from Fe 2p XPS spectra of MAOM (PDF)

## ■ AUTHOR INFORMATION


### Corresponding Authors

**Jie Jiang** − *College of Environmental Science and Engineering, Beijing Forestry University, Beijing 100083, China;* orcid.org/0000-0002-8381-2404; Email: jiangjie@bjfu.edu.cn

**Zhen Yang** − *State Key Laboratory of Regional and Urban Ecology, Research Center for Eco-environmental Sciences, Chinese Academy of Sciences, Beijing 100085, China;* orcid.org/0000-0001-7282-9190; Email: zhenyang@rcees.ac.cn

### Authors

**Xi Zhang** − *College of Environmental Science and Engineering, Beijing Forestry University, Beijing 100083, China;* orcid.org/0009-0000-3732-3741

**Andreas Kappler** − *Geomicrobiology, Department of Geosciences, Tuebingen 72076, Germany; Cluster of Excellence: EXC 2124: Controlling Microbes to Fight Infection, Tuebingen 72076, Germany;* orcid.org/0000-0002-3558-9500

**Qian Tian** − *State Key Laboratory of Regional and Urban Ecology, Research Center for Eco-environmental Sciences, Chinese Academy of Sciences, Beijing 100085, China; UCAS, College of Resource and Environment, Beijing 100085, China*

**Tian ran Sun** − *State Key Laboratory of Regional and Urban Ecology, Research Center for Eco-environmental Sciences, Chinese Academy of Sciences, Beijing 100085, China; UCAS, College of Resource and Environment, Beijing 100085, China;* orcid.org/0000-0001-8679-1285

Complete contact information is available at: https://pubs.acs.org/10.1021/acsearthspacechem.6c00141


### Notes

The authors declare no competing financial interest.

## ■ ACKNOWLEDGMENTS

This research was supported by grants from the National Natural Science Foundation of China (Grant Nos. 42407297, 42477048).

## ■ REFERENCES


(1) Angst, G.; Mueller, K. E.; Castellano, M. J.; Vogel, C.; Wiesmeier, M.; Mueller, C. W. Unlocking complex soil systems as carbon sinks: Multi-pool management as the key. *Nat. Commun.* **2023**, *14* (1), 2967.

(2) Cotrufo, M. F.; Ranalli, M. G.; Haddix, M. L.; Six, J.; Lugato, E. Soil carbon storage informed by particulate and mineral-associated organic matter. *Nat. Geosci.* **2019**, *12* (12), 989−994.

(3) Mueller, C. W.; Kögel-Knabner, I. Soil organic carbon stocks, distribution, and composition affected by historic land use changes on adjacent sites. *Biol. Fertil. Soils* **2009**, *45* (4), 347−359.

(4) Witzgall, K.; Vidal, A.; Schubert, D. I.; Höschen, C.; Schweizer, S. A.; Buegger, F.; Pouteau, V.; Chenu, C.; Mueller, C. W. Particulate organic matter as a functional soil component for persistent soil organic carbon. *Nat. Commun.* **2021**, *12* (1), 4115.

(5) Aeschbacher, M.; Vergari, D.; Schwarzenbach, R. P.; Sander, M. Electrochemical Analysis of Proton and Electron Transfer Equilibria of the Reducible Moieties in Humic Acids. *Environ. Sci. Technol.* **2011**, *45* (19), 8385−8394.
(6) Anderson, C. G.; Goebel, G. M.; Tfaily, M. M.; Fox, P. M.; Nico, P. S.; Fendorf, S.; Keiluweit, M. Molecular nature of mineral-organic associations within redox-active mountainous floodplain sediments. *ACS Earth Space Chem.* **2023**, *7* (9), 1623−1634.
(7) Gao, C. Y.; Sander, M.; Agethen, S.; Knorr, K. H. Electron accepting capacity of dissolved and particulate organic matter control CO2 and CH4 formation in peat soils. *Geochim. Cosmochim. Acta* **2019**, *245*, 266−277.
(8) Guth, P.; Gao, C. Y.; Knorr, K. H. Electron accepting capacities of a wide variety of peat materials from around the globe similarly explain $CO_2$ and $CH_4$ formation. *Global Biogeochem. Cycles* **2023**, *37* (1), No. e2022GB007459.
(9) Joshi, P.; Thomasarrigo, L. K.; Sawwa, D.; Sauter, L.; Kappler, A. Complexation by particulate organic matter alters iron redox behavior. *ACS Earth Space Chem.* **2024**, *8* (2), 310−322.
(10) LaCroix, R. E.; Walpen, N.; Sander, M.; Tfaily, M. M.; Blanchard, J. L.; Keiluweit, M. Long-term warming decreases redox capacity of soil organic matter. *Environ. Sci. Technol. Lett.* **2021**, *8* (1), 92−97.
(11) Bölscher, T.; Cardon, Z. G.; Arredondo, M. G.; Grand, S.; Griffen, G.; Hestrin, R.; Imboden, J.; Jamoteau, F.; Lacroix, E. M.; Castro, S. P.; Persson, P.; Riley, W. J.; Keiluweit, M. Vulnerability of mineral-organic associations in the rhizosphere. *Nat. Commun.* **2025**, *16* (1), 5527.
(12) Coward, E. K.; Thompson, A. T.; Plante, A. F. Iron-mediated mineralogical control of organic matter accumulation in tropical soils. *Geoderma* **2017**, *306*, 206−216.
(13) Feng, X. J.; Zhao, Y. P.; Wang, H. Q.; Liu, C. Z. Iron-Organic Carbon Interactions in Wetlands: Implications for Wetland Carbon Preservation Under Global Changes. *Global Change Biol.* **2025**, *31* (6), No. e70300.
(14) Wang, S.; Liu, T.; Zhu, E.; He, C.; Shi, Q.; Feng, X. Potential retention of dissolved organic matter by soil minerals during wetland water-table fluctuations. *Water Res.* **2024**, *254*, 121412.
(15) Wang, Y. Y.; Liu, X. Q.; Zhang, X. Y.; Dai, G. H.; Wang, Z. H.; Feng, X. J. Evaluating wetland soil carbon stability related to iron transformation during redox oscillations. *Geoderma* **2022**, *428*, 116222.
(16) Li, Z. C.; Li, X. Y.; Jiao, B. Q.; Yang, Y. S.; Wang, H. Y.; Gu, L.; Ai, H. A.; Cheng, H.; Cheng, S. Redox oscillations in riparian zone stimulate carbon loss by enhancing microbial respiration. *Water Res.* **2026**, *296*, 125672.
(17) Liu, F. H.; Ding, Y. Y.; Liu, J.; Latif, J.; Qin, J. J.; Tian, S. X.; Sun, S. Y.; Guan, B. T.; Zhu, K. C.; Jia, H. Z. The effect of redox fluctuation on carbon mineralization in riparian soil: An analysis of the hotspot zone of reactive oxygen species production. *Water Res.* **2024**, *265*, 122294.
(18) Wallace, C. D.; Soltanian, M. R. Underlying riparian lithology controls redox dynamics during stage-driven mixing. *Journal of Hydrology* **2021**, *595*, 126035.
(19) Sun, L. R.; Jiang, M. X.; Li, M.; Wang, X. G.; Han, Y. F.; Chen, X. N. Increased light intensity mitigates $CO_2$ and $CH_4$ emissions from paddy soil by mediating iron redox cycling coupled with organic carbon transformation. *Agronomy-Basel* **2025**, *15* (5), 1137.
(20) Tan, W. B.; Wang, G. A.; Zhao, X. Y.; Dang, Q. L.; Li, R. F.; Xi, B. D.; Jiang, J.; Zhang, H.; Li, D.; Cui, D. Y.; Jia, Y. F. Molecular-weight-dependent redox cycling of humic substances of paddy soils over successive anoxic and oxic alternations. *Land Degradation & Development* **2019**, *30* (9), 1130−1144.
(21) Maisch, M.; Lueder, U.; Kappler, A.; Schmidt, C. Iron Lung: How Rice Roots Induce Iron Redox Changes in the Rhizosphere and Create Niches for Microaerophilic Fe(II)-Oxidizing Bacteria. *Environ. Sci. Technol. Lett.* **2019**, *6* (10), 600−605.
(22) Watanabe, T.; Kato, K.; Kawaguchi, K.; Oga, T.; Ban, Y.; Otoidobiga, C. H.; Sawadogo, A.; Wonni, I.; Ouedraogo, L. S.; Zongo, J. D.; Dianou, D.; Asakawa, S. Investigation of iron-reducing and iron-oxidizing bacterial communities in the rice rhizosphere of iron-toxic paddy field: a case study in Burkina Faso, West Africa. *Soil Sci. Plant Nutr.* **2023**, *69* (5−6), 283−293.
(23) Qin, B.; Huang, Y.; Liu, T.; Wu, Y.; Li, F. Dissolved organic matter (DOM) enhances the competitiveness of weak exoelectrogens in a soil electroactive biofilm. *Carbon Res.* **2024**, *3* (1), 34.
(24) Yang, P. J.; Jiang, T.; Cong, Z. Y.; Liu, G. L.; Guo, Y. Y.; Liu, Y. W.; Shi, J. B.; Hu, L. G.; Yin, Y. G.; Cai, Y.; Jiang, G. B. Loss and increase of the electron exchange capacity of natural organic matter during its reduction and reoxidation: The role of quinone and nonquinone moieties. *Environ. Sci. Technol.* **2022**, *56* (10), 6744−6753.
(25) Bhattacharyya, A.; Campbell, A. N.; Tfaily, M. M.; Lin, Y.; Kukkadapu, R. K.; Silver, W. L.; Nico, P. S.; Pett-Ridge, J. Redox fluctuations control the coupled cycling of iron and carbon in tropical forest soils. *Environ. Sci. Technol.* **2018**, *52* (24), 14129−14139.
(26) Kleber, M.; Sollins, P.; Sutton, R. A conceptual model of organo-mineral interactions in soils: Self-assembly of organic molecular fragments into zonal structures on mineral surfaces. *Biogeochemistry* **2007**, *85* (1), 9−24.
(27) Ma, H.; Thompson, A.; Hall, S. J.; Wang, J. L.; Xiao, Y. Q.; Liu, C. Q.; Chen, C. M. Enrichment of metastable iron minerals in global coastal wetlands. *Nat. Geosci.* **2025**, *18* (9), 885−892.
(28) Thompson, A.; Chadwick, O. A.; Rancourt, D. G.; Chorover, J. Iron-oxide crystallinity increases during soil redox oscillations. *Geochim. Cosmochim. Acta* **2006**, *70* (7), 1710−1727.
(29) Tishchenko, V.; Meile, C.; Scherer, M. M.; Pasakarnis, T. S.; Thompson, A. $Fe^{2+}$ catalyzed iron atom exchange and re-crystallization in a tropical soil. *Geochim. Cosmochim. Acta* **2015**, *148*, 191−202.
(30) Brazhkin, V. V. Metastable phases and 'metastable' phase diagrams. *J. Phys.: Condens. Matter* **2006**, *18* (42), 9643−9650.
(31) Peiffer, S.; Kappler, A.; Haderlein, S. B.; Schmidt, C.; Byrne, J. M.; Kleindienst, S.; Vogt, C.; Richnow, H. H.; Obst, M.; Angenent, L. T.; Bryce, C.; McCammon, C.; Planer-Friedrich, B. A biogeochemical-hydrological framework for the role of redox-active compounds in aquatic systems. *Nat. Geosci.* **2021**, *14* (5), 264−272.
(32) Dong, H. L.; Zeng, Q.; Sheng, Y. Z.; Chen, C. M.; Yu, G. H.; Kappler, A. Coupled iron cycling and organic matter transformation across redox interfaces. *Nat. Rev. Earth Environ.* **2023**, *4* (9), 659−673.
(33) Gee, G. W.; Or, D. 2.4 Particle-Size Analysis. In *Methods of Soil Analysis*, 2002; pp 255−293.
(34) Gentsch, N.; Wild, B.; Mikutta, R.; Capek, P.; Diáková, K.; Schrumpf, M.; Turner, S.; Minnich, C.; Schaarschmidt, F.; Shibistova, O.; Schnecker, J.; Urich, T.; Gittel, A.; Santrucková, H.; Bárta, J.; Lashchinskiy, N.; Fuss, R.; Richter, A.; Guggenberger, G. Temperature response of permafrost soil carbon is attenuated by mineral protection. *Global Change Biol.* **2018**, *24* (8), 3401−3415.
(35) Lalonde, K.; Mucci, A.; Ouellet, A.; Gélinas, Y. Preservation of organic matter in sediments promoted by iron. *Nature* **2012**, *483* (7388), 198−200.
(36) Aller, R. C.; Mackin, J. E.; Cox, R. T. Diagenesis of Fe and S in Amazon inner shelf muds: apparent dominance of Fe reduction and implications for the genesis of ironstones. *Cont. Shelf Res.* **1986**, *6* (1−2), 263−289.
(37) Patzner, M. S.; Mueller, C. W.; Malusova, M.; Baur, M.; Nikeleit, V.; Scholten, T.; Hoeschen, C.; Byrne, J. M.; Borch, T.; Kappler, A.; Bryce, C. Iron mineral dissolution releases iron and associated organic carbon during permafrost thaw. *Nat. Commun.* **2020**, *11* (1), 6329.
(38) Liu, F. T.; Qin, S. Q.; Fang, K.; Chen, L. Y.; Peng, Y. F.; Smith, P.; Yang, Y. H. Divergent changes in particulate and mineral-associated organic carbon upon permafrost thaw. *Nat. Commun.* **2022**, *13* (1), 5073.
(39) Lavallee, J. M.; Soong, J. L.; Cotrufo, M. F. Conceptualizing soil organic matter into particulate and mineral-associated forms to

address global change in the 21st century. *Global Change Biol.* **2020**, *26* (1), 261−273.
(40) Benz, M.; Schink, B.; Brune, A. Humic Acid Reduction by Propionibacterium freudenreichii and Other Fermenting Bacteria. *Appl. Environ. Microbiol.* **1998**, *64* (11), 4507−4512.
(41) Kappler, A.; Benz, M.; Schink, B.; Brune, A. Electron shuttling via humic acids in microbial iron(III) reduction in a freshwater sediment. *FEMS Microbiol. Ecol.* **2004**, *47* (1), 85−92.
(42) Yang, Z.; Kappler, A.; Jiang, J. Reducing Capacities and Distribution of Redox-Active Functional Groups in Low Molecular Weight Fractions of Humic Acids. *Environ. Sci. Technol.* **2016**, *50* (22), 12105−12113.
(43) Gorski, C. A.; Klüpfel, L. E.; Voegelin, A.; Sander, M.; Hofstetter, T. B. Redox properties of structural Fe in clay minerals: 3. Relationships between smectite redox and structural properties. *Environ. Sci. Technol.* **2013**, *47* (23), 13477−13485.
(44) Sun, T. R.; Levin, B. D. A.; Schmidt, M. P.; Guzman, J. J. L.; Enders, A.; Martínez, C. E.; Muller, D. A.; Angenent, L. T.; Lehmann, J. Simultaneous Quantification of Electron Transfer by Carbon Matrices and Functional Groups in Pyrogenic Carbon. *Environ. Sci. Technol.* **2018**, *52* (15), 8538−8547.
(45) Joshi, P.; Schroth, M. H.; Sander, M. Redox properties of peat particulate organic matter: Quantification of electron accepting capacities and assessment of electron transfer reversibility. *J. Geophys. Res. Biogeosciences* **2021**, *126* (8), No. e2021JG006329.
(46) Tan, W. B.; Xi, B. D.; Wang, G. A.; Jiang, J.; He, X. S.; Mao, X. H.; Gao, R. T.; Huang, C. H.; Zhang, H.; Li, D.; Jia, Y. F.; Yuan, Y.; Zhao, X. Y. Increased Electron-Accepting and Decreased Electron-Donating Capacities of Soil Humic Substances in Response to Increasing Temperature. *Environ. Sci. Technol.* **2017**, *51* (6), 3176−3186.
(47) Aeschbacher, M.; Sander, M.; Schwarzenbach, R. P. Novel electrochemical approach to assess the redox properties of humic substances. *Environ. Sci. Technol.* **2010**, *44* (1), 87−93.
(48) Yang, P. J.; Jiang, T.; Cong, Z. Y.; Liu, G. L.; Guo, Y. Y.; Liu, Y. W.; Shi, J. B.; Hu, L. G.; Yin, Y. G.; Cai, Y.; Jiang, G. B. Loss and Increase of the Electron Exchange Capacity of NaturalOrganic Matter during Its Reduction and Reoxidation: The Role ofQuinone and Nonquinone Moieties. *Environ. Sci. Technol.* **2022**, *56* (10), 6744−6753.
(49) Aeschbacher, M.; Graf, C.; Schwarzenbach, R. P.; Sander, M. Antioxidant Properties of Humic Substances. *Environ. Sci. Technol.* **2012**, *46* (9), 4916−4925.
(50) Peng, C.; Bryce, C.; Sundman, A.; Kappler, A. Cryptic Cycling of Complexes Containing Fe(III) and Organic Matter by Phototrophic Fe(II)-Oxidizing Bacteria. *Appl. Environ. Microbiol.* **2019**, *85* (8), e02826−18.
(51) Patzner, M. S.; Logan, M.; McKenna, A. M.; Young, R. B.; Zhou, Z.; Joss, H.; Mueller, C. W.; Hoeschen, C.; Scholten, T.; Straub, D.; Kleindienst, S.; Borch, T.; Kappler, A.; Bryce, C. Microbial iron cycling during palsa hillslope collapse promotes greenhouse gas emissions before complete permafrost thaw. *Commun. Earth Environ.* **2022**, *3* (1), 76.
(52) Vincent, S.; Jennerjahn, T.; Ramasamy, K. *Biogeocycling of nutrients (C, N, P, S, and Fe) and implications on greenhouse gas emissions. Microbial communities in coastal sediments*. Vincent, S. G. T.; Jennerjahn, T. C.; Ramasamy, K., Eds. (Elsevier, Amsterdam) 2021, 119−145.
(53) Tolunay, D.; Ergut, G.; Simon, L.; Erkens, G.; Kowalchuk, G. A.; Hefting, M. M. Iron and sulphur regulate carbon dioxide emissions in drained coastal peatlands of The Netherlands. *Biogeochemistry* **2026**, *169* (1), 8.
(54) Voggenreiter, E.; Thomasarrigo, L.; Kilian, J.; Straub, D.; Friedel, M.; Stahl, M.; Kappler, A.; Joshi, P. Reduction of iron-organic carbon associations shifts net greenhouse gas release after initial permafrost thaw. *Soil Biol. Biochem.* **2025**, *203*, 109735.
(55) Shi, L.; Squier, T. C.; Zachara, J. M.; Fredrickson, J. K. Respiration of metal (hydr)oxides by Shewanella and Geobacter:: a key role for multihaem c-type cytochromes. *Mol. Microbiol.* **2007**, *65* (1), 12−20.
(56) Cabugao, K. G. M.; Gushgari-Doyle, S.; Chacon, S. S.; Wu, X. Q.; Bhattacharyya, A.; Bouskill, N.; Chakraborty, R. Characterizing Natural Organic Matter Transformations by Microbial Communities in Terrestrial Subsurface Ecosystems: A Critical Review of Analytical Techniques and Challenges. *Front. Microbiol.* **2022**, *13*, 864895.
(57) White, G. F.; Shi, Z.; Shi, L.; Wang, Z. M.; Dohnalkova, A. C.; Marshall, M. J.; Fredrickson, J. K.; Zachara, J. M.; Butt, J. N.; Richardson, D. J.; Clarke, T. A. Rapid electron exchange between surface-exposed bacterial cytochromes and Fe(III) minerals. *Proc. Natl. Acad. Sci. U.S.A.* **2013**, *110* (16), 6346−6351.
(58) Zhang, S. M.; Wang, F. S.; Wang, Y. C.; Chen, X. P.; Xu, P. F.; Miao, H. C. Shifts of soil archaeal nitrification and methanogenesis with elevation in water level fluctuation zone of the three Gorges Reservoir, China. *J. Environ. Manage.* **2023**, *339*, 117871.
(59) Xu, Z. B.; Tsang, D. C. W. Mineral-mediated stability of organic carbon in soil and relevant interaction mechanisms. *Eco-Environment & Health* **2024**, *3* (1), 59−76.
(60) Cotrufo, M. F.; Lavallee, J. M. Soil organic matter formation, persistence, and functioning: A synthesis of current understanding to inform its conservation and regeneration. In *Advances in Agronomy*; Sparks, D. L., Ed., 2022; Vol. *172*, pp 1−66. Vol. 172.
(61) Zhang, D. L.; Liu, X. L.; Dong, H. L. Enhanced Organic Matter Sequestration and Phosphate Adsorption by Fe Oxides Generated from Abiotic Fe(II) Oxidation in the Presence of Heavy Metals. *Environ. Sci. Technol.* **2025**, *59* (23), 11820−11828.
(62) Chen, C. M.; Dynes, J. J.; Wang, J.; Sparks, D. L. Properties of Fe-Organic Matter Associations via Coprecipitation versus Adsorption. *Environ. Sci. Technol.* **2014**, *48* (23), 13751−13759.
(63) Chen, C. M.; Hall, S. J.; Coward, E.; Thompson, A. Iron-mediated organic matter decomposition in humid soils can counteract protection. *Nat. Commun.* **2020**, *11* (1), 2255.
(64) Chen, Y. R.; Dong, L.; Sui, W. K.; Niu, M. Y.; Cui, X. Q.; Hinrichs, K. U.; Wang, F. P. Cycling and persistence of iron-bound organic carbon in subseafloor sediments. *Nat. Commun.* **2024**, *15* (1), 6370.
(65) Ni, B. B.; Yu, X. F.; Duan, X.; Zou, Y. C. Wetland soil organic carbon balance is reversed by old carbon and iron oxide additions. *Front. Microbiol.* **2024**, *14*, 1327265.
(66) Yang, L.; Zou, Y. C.; Jia, Z. J.; Luo, Y.; Qin, L.; Jiang, M.; Yu, Z. C. Iron reduction promotes carbon mineralization and nutrient release of iron-associated organic matter in anoxic environments. *Water Res.* **2025**, *284*, 124032.
(67) Li, Z. C.; Li, X. Y.; Yang, Y. S.; Li, J. Z.; Wang, H. Y.; Tang, L. Z.; Gu, L.; Ai, H. A.; Jiao, B. Q.; Pan, W. L. Soil Organic Matter Modulation during Redox Oscillations: Insights from Iron Speciation and Microbial Metabolism. *Environ. Sci. Technol.* **2026**, *60* (9), 7111−7122.